AGU PUBLICATIONS

Water Resources Research

RESEARCH ARTICLE

10.1002/2013WR015243

Key Points:
- Snowmelt explained 68 and 44% of stream nitrate at CA and CO sites, respectively
- Stream nitrate at the CA and CO sites exhibited opposite responses to snowmelt
- Hydrochemical response to snowmelt was strongly affected by flow paths

Supporting Information:
- Readme
- Supporting Figure S1

Correspondence to:
N. Molotch,
noah.molotch@colorado.edu

Citation:
Perrot, D., N. P. Molotch, M. W. Williams, S. M. Jepsen, and J. O. Sickman (2014), Relationships between stream nitrate concentration and spatially distributed snowmelt in high-elevation catchments of the western U.S.., *Water Resour. Res.*, *50*, 8694–8713, doi:10.1002/2013WR015243.

Received 31 DEC 2013
Accepted 30 SEP 2014
Accepted article online 6 OCT 2014
Published online 12 NOV 2014

Relationships between stream nitrate concentration and spatially distributed snowmelt in high-elevation catchments of the western U.S.

Danielle Perrot[1], Noah P. Molotch[1,2], Mark W. Williams[1], Steven M. Jepsen[3], and James O. Sickman[4]

[1]Department of Geography, Institute of Arctic and Alpine Research, University of Colorado at Boulder, Boulder, Colorado, USA, [2]Jet Propulsion Laboratory, California Institute of Technology, Pasadena, California, USA, [3]Sierra Nevada Research Institute, University of California, Merced, California, USA, [4]Department of Environmental Sciences, University of California, Riverside, California, USA

Abstract This study compares stream nitrate (NO_3^-) concentrations to spatially distributed snowmelt in two alpine catchments, the Green Lakes Valley, Colorado (GLV4) and Tokopah Basin, California (TOK). A snow water equivalent reconstruction model and Landsat 5 and 7 snow cover data were used to estimate daily snowmelt at 30 m spatial resolution in order to derive indices of new snowmelt areas (NSAs). Estimates of NSA were then used to explain the NO_3^- flushing behavior for each basin over a 12 year period (1996–2007). To identify the optimal method for defining NSAs and elucidate mechanisms underlying catchment NO_3^- flushing, we conducted a series of regression analyses using multiple thresholds of snowmelt based on temporal and volumetric metrics. NSA indices defined by volume of snowmelt (e.g., snowmelt $\leq$ 30 cm) rather than snowmelt duration (e.g., snowmelt $\leq$ 9 days) were the best predictors of stream NO_3^- concentrations. The NSA indices were better correlated with stream NO_3^- concentration in TOK (average $R^2 = 0.68$) versus GLV4 (average $R^2 = 0.44$). Positive relationships between NSA and stream NO_3^- concentration were observed in TOK with peak stream NO_3^- concentration occurring on the rising limb of snowmelt. Positive and negative relationships between NSA and stream NO_3^- concentration were found in GLV4 with peak stream NO_3^- concentration occurring as NSA expands. Consistent with previous works, the contrasting NO_3^- flushing behavior suggests that streamflow in TOK was primarily influenced by overland flow and shallow subsurface flow, whereas GLV4 appeared to be more strongly influenced by deeper subsurface flow paths.

1. Introduction

Delivery and biological attenuation of atmospheric nitrogenous compounds in high-elevation ecosystems are modulated by snowmelt and biogeochemical processes within catchment soils, both of which are sensitive to changes in regional climate. The timing and magnitude of snow accumulation and snowmelt plays an important role in catchment N cycling by influencing microbial processes in subnivean soils [*Brooks and Williams*, 1999; *Sickman et al*., 2001, 2003a] and by flushing solutes from hillslopes to streams [*Meixner and Bales*, 2003; *Sickman et al*., 2001; *Williams et al*., 1996a]. Tight coupling between hydrology and biogeochemical processes in soils is the basis for the concept of "Hot Spots—Hot Moments," proposed by *McClain et al*. [2003] and used to describe the spatial and temporal variability of carbon and nitrogen reactions in watersheds. The concept stresses the importance of water flow paths in creating locations (Hot Spots) of accelerated reaction rates during transient events (Hot Moments) such as snowmelt.

High-elevation ecosystems (elevation > 2500 m) exhibit relatively large episodic releases of NO_3^- in response to hydrologic flushing driven by a variety of processes [*Campbell et al*., 2002; *Sickman et al*., 2003a; *Williams and Melack*, 1991b]. The transfer of NO_3^- from the snowpack is complicated by preferential elution of solutes in snow [*Johannessen and Henriksen*, 1978; *Bales et al*., 1989], such that the NO_3^- concentration in the first 20% of meltwater leaving the snowpack may be several times greater than the bulk snowpack concentration [*Williams et al*., 1996b]. The path of NO_3^- from the snowpack to the soil, plants, lakes, or streams also depends on basin topography and subsurface flow paths [*Liu et al*., 2004; *Molotch et al*., 2008; *Sickman et al*., 2002; *Williams et al*., 1996c]. Soils can act as a source and/or a sink of NO_3^-, depending on soil physiochemical characteristics and biological productivity. For example, multiple studies have indicated the

importance of inorganic N production in snow-covered soils and mineralization of atmospherically deposited ammonium to nitrate at Niwot Ridge, CO [*Brooks and Williams*, 1999; *Williams et al*., 1996b; *Barnes et al*., 2013]. NO_3^- immobilization and assimilation in the terrestrial environment are affected by vegetation and microbial populations [*Heuer et al*., 1999], but infiltrating rain or snowmelt can also flush microbially produced NO_3^- from the terrestrial environment to streams and lakes. In the Tokopah basin in the Sierra Nevada, the magnitude of springtime NO_3^- pulses are related to the timing of snowmelt and amount of snowpack SWE [*Sickman et al*., 2001]; stable isotope measurements of nitrate demonstrate that 70–75% of the exported NO_3^- is derived from soils and about 20–25% is snowpack NO_3^- [*Sickman et al*., 2003a, 2003b]. Talus plays an important role as a source of microbial NO_3^- [*Liu et al*., 2004; *Williams et al*., 1997], because retention of inorganic N is lower in talus than soils because of less vegetation and lower biological N demand. Hence, the distribution of snowmelt and the flow paths connecting hillslopes to streams are likely to strongly influence episodic NO_3^- flushing in high-elevation catchments at fine spatial and temporal scales [*Williams et al*., 1996a; *Sickman et al*., 2002; *Burns*, 2003; *Elser et al*., 2009].

The concept of variable source area (VSA) hydrology [*Hewlett and Hibbert*, 1967] applies to catchments where infiltration rates are greater than rainfall and/or snowmelt rates, and overland flow paths are generated primarily by precipitation falling onto saturated regions of a watershed (i.e., saturation-excess overland flow). Areas of saturation vary with the intensity and duration of rainfall, growing in size as rainfall increases and causing an expansion of the channel network and greater hydrologic connectivity within a catchment. Similar dynamics may operate in snowmelt-dominated catchments, where spatiotemporal variations in snowmelt runoff, rather than rainfall, drive patterns of runoff.

The concepts of VSA hydrology have merged with watershed biogeochemistry to help explain patterns of hydrochemistry in streams. *Creed et al*. [1996] and *Creed and Band* [1998a, 1998b] used VSA regulation of solute flushing from soils to explain variations in NO_3^- export from temperate watersheds in Ontario, Canada. In these catchments, NO_3^- in the upper soil layers was episodically flushed when infiltrating snowmelt caused the water table to rise to the soil surface, generating return flow to streams [*Dunne and Leopold*, 1978]. Since the amount of NO_3^- that can be eluted from the snowpack or flushed from soils is finite, the rate of catchment-scale NO_3^- flushing was observed to be proportional to the production rate of newly saturated areas of the catchment. When saturated regions were rapidly produced by expanding new snowmelt area (NSA), NO_3^- levels in catchment streams rose proportionally. Once snowmelt had occurred in all areas of a catchment, NO_3^- levels in catchment streams declined in an exponential fashion as reservoirs of mobile NO_3^- were depleted by dilute snowmelt waters.

Understanding of the relationship between episodic NO_3^- flushing and hydrologic flow paths during snowmelt has been limited by uncertainty in snowmelt distribution at finer spatial scales. Recent advances in remote sensing techniques [e.g., *Painter et al*., 2003, 2009] have improved snowmelt modeling in mountainous areas. The coupling of remotely sensed fractional snow-covered area (SCA) data with spatially distributed snowpack modeling has improved estimates of snowmelt by using a hindcasting technique [*Cline et al*., 1998; *Jepsen et al*., 2012; *Marks et al*., 1999; *Martinec and Rango*, 1981; *Molotch et al*., 2004]. This reconstruction approach, which we use in this study, sums modeled snowmelt at the pixel scale for the duration of satellite-observed snow cover and has been utilized in a variety of applications [*Cline et al*., 1998; *Jepsen et al*., 2012; *Martinec and Rango*, 1981; *Molotch et al*., 2008; *Molotch*, 2009]. The approach is particularly useful in alpine areas as it does not rely on precipitation forcings which are highly uncertain in mountain catchments. Including spatially distributed snowmelt estimates in hydrochemical analyses allows for the detection of the spatiotemporal variability in the extent of areas contributing to snowmelt and/or NO_3^- to streams.

We are interested in whether varying spatiotemporal patterns of snowmelt results in differences in stream nitrate concentrations. We hypothesize that spatiotemporal variability in snowmelt is correlated with stream nitrate concentration. In this context, we hypothesize that years with high spatial variability in the timing of snowmelt onset have lower peak stream nitrate concentrations as stream waters with high nitrate concentration from new snowmelt areas are diluted by older snowmelt areas that have lower concentration of nitrate. In this study, we utilize 12 years of hydrometeorological and hydrochemical observations combined with a spatially distributed snowmelt model to link stream NO_3^- response to spatially distributed snowmelt in two alpine catchments, one from the Sierra Nevada of California (Tokopah basin) and the second from the Rocky Mountains of Colorado (Green Lakes Valley 4 catchment). Our overarching questions are:

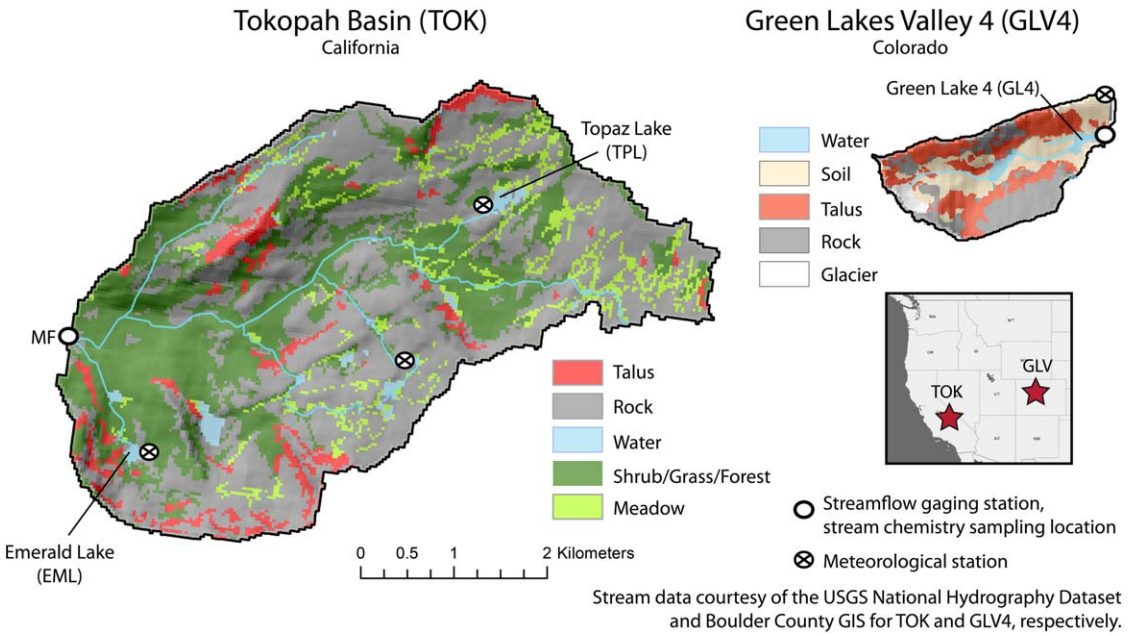

Figure 1. Landcover maps and locations of Tokopah Basin, CA and Green Lakes Valley 4, CO (USA). The locations of discharge, stream chemistry (black circles), and meteorological measurements (circle-hash) are also displayed.

1. Do spatiotemporal patterns of snowmelt influence temporal variability in stream NO_3^- concentrations in high-elevation catchments?
2. How do these two basins differ with respect to relationships between spatially distributed snowmelt and stream NO_3^- concentrations?

Within this framework, we explore different NSA indices based on flushing time and volume and quantify their ability to predict NO_3^- concentrations in streams during snowmelt. These questions allow us to infer underlying processes controlling nitrate export in these systems, particularly related to routing, residence times, and storage. Our study contributes to better understanding of catchment-scale nitrogen dynamics with implications for predicting the impacts of climate change on high-elevation ecosystems.

2. Study Areas

The Green Lakes 4 Valley catchment (henceforth GLV4) (40°03′N, 105°35′W) is an east-facing 2.2 km^2 alpine watershed located in the Colorado Front Range, approximately 60 km northwest from Denver, Colorado (Figure 1). The catchment is generally representative of alpine areas in this region [*Caine*, 1995] with an elevation range of 3515–4084 m and an average slope of 28° [*Jepsen et al.*, 2012]. GLV4 landcover consists of 29% exposed bedrock, 29% soils, 33% talus, and 9% glacier [*Erickson et al.*, 2005; *Meixner et al.*, 2000]. GLV4 is characterized by a continental climate regime, with a mean annual temperature of −3.7°C and 80% of precipitation occurring as snow [*Williams et al.*, 1996c]. Snowmelt typically begins in early to mid-May, with streamflow peaking in late-June [*Caine*, 1995]. GLV4 is located within the Niwot Ridge Long-Term Ecological Research site (LTER, http://niwot.colorado.edu/index.php) and the Boulder Creek watershed, and there is a continuous climate record extending back to the 1950s [*Caine*, 1995]. A colocated National Atmospheric Deposition Program collector at the Niwot Ridge Saddle site (CO02) provides a continuous record of precipitation and atmospheric deposition of solutes dating back to the early 1980s. GLV4 stream discharge is measured daily, and chemistry samples are collected weekly at the outflow of Green Lake 4 (GL4) from the time of initial snowmelt to the onset of lake-ice formation in the fall; samples are collected monthly during the winter by drilling through the lake ice.

The Tokopah Basin (henceforth TOK) is an alpine basin located on the west side of the Sierra Nevada mountain range in Sequoia National Park, California (Figure 1). TOK is approximately 19.1 km^2, with an elevation range spanning 2621–3416 m and an average slope of 17°. Its area is nearly nine times greater than that of

Table 1. Statistics of Snow Surveys Conducted in TOK and GLV4 Between 1996 and 2007[a]

	TOK						GLV4					
Year	Date	d_{ave}	N_d	ρ_{ave}	N_ρ	CV	Date	d_{ave}	N_d	ρ_{ave}	N_ρ	CV
1996	11 Apr	273	319	454	3	0.39	4 May	-	-	382	6	-
1997	9 Apr	256	429	465	10	0.37	14 May	256[b]	193[b]	398	5	0.73[b]
1998	6 May	361	352	467	42 (40)	0.32	20 May	242[b]	370[b]	494	5	0.69[b]
1999	17 Apr	169	204	406	15 (12)	0.38	12 May	221[b]	532[b]	359	4	0.88[b]
2000	15 Apr	256	11	480	2 (1)	0.19	3 May	213[b]	655[b]	461	4	0.88[b]
2001	28 Apr	191	54	440	1	0.29	9 May	188[b]	511[b]	419	4	0.74[b]
2002	30 Apr	176	95	-	-	0.42	1 May	123[b]	447[b]	386	2	1.09[b]
2003	-	-	-	-	-	-	14 May	222[b]	527[b]	376	5	0.75[b]
2004	15 Apr	174	86	-	-	0.5	12 May	132	517	445	5	1
2005	2 Apr	405	21	403	1	0.38	10 May	215	427	380	3	0.75
2006	-	-	-	-	-	-	11 May	152	483	405	1	0.98
2007	3 Apr	133	83	-	-	0.37	10 May	124	695	418	5	1.06

[a]Reproduced from *Jepsen et al.* [2012]. Symbols are as follows: d_{ave}, mean depth (cm); N_d, number of depth measurements; ρ_{ave}, mean snow density (kg m^{-3}); N_ρ, number of density measurements (number of Federal sampler cores in parentheses); CV, spatial coefficient of variation. A dash indicates no data.

[b]Data from *Erickson et al.* [2005].

GLV4. Basin land cover units include 51% exposed granitic bedrock, 5% talus, and 40% vegetated soils (meadows and shrub, grass, and forested areas labeled in Figure 1) at the lower elevations adjacent to streams [*Jepsen et al.*, 2012]. TOK is influenced by Mediterranean, maritime climate dynamics, with most precipitation (75–90%) falling as snow during the winter months [*Tonnessen*, 1991]. Annual precipitation varies from less than 1 m to greater than 2 m [*Jepsen et al.*, 2012; *Williams and Melack*, 1991a], and annual snow water equivalence varies from less than 0.5 to 1.8 m [*Jepsen et al.*, 2012]. Snowmelt typically begins in early April [*Molotch and Bales*, 2006] and discharge typically peaks in June. Groundwater inputs keep the lower reaches of the river flowing during the late summer, but by late autumn, the entire river dries up in most years. Hydrograph separation studies suggest that old water makes up about 10% of annual discharge and that the TOK lacks a well-developed groundwater system [*Kramer-Huth et al.*, 2004]. Stream chemistry and stream discharge measurements are made at the Marble Fork gaging station at the basin outflow since 1992. Additional meteorological, radiation, precipitation, and gaging stations are located nearby in the Emerald Lake and Topaz Lake subcatchments as well as at the M3 meteorological station with records dating back to July 1985 (http://ccb.ucr.edu/emeraldlake/sites.html).

3. Methods

3.1. Physical and Chemical Measurements of the Snowpack

Snow survey data were used to provide an independent check on the snowmelt model [*Jepsen et al.*, 2012]. Snow depth was measured in both basins at about the time of maximum accumulation each year using hand probes and GPS units for location (Table 1). The average number of individual snow depth measurements made during each annual snow survey was 137 for TOK and 471 for GLV4 [*Jepsen et al.*, 2012]. Snowpit locations were distributed across elevational gradients and variable aspects throughout each basin. Snowpits were dug from the snow surface to the ground at maximum accumulation each year and sampled for physical and chemical parameters. Samples were collected on the north-facing wall of the snowpit to shade the sampling face from direct sunlight, which can quickly change snow properties. In each snowpit, snow density was measured using a 1000 cm^3 stainless steel cutter at 10 cm intervals from the snow surface to ground. These protocols were initially developed for TOK in the 1980s and then applied to GLV4 and Niwot Ridge beginning in the early 1990s [*Williams and Melack*, 1991a, 1991b]. In TOK, some additional measurements of snow density were made using a Federal Sampler [*Jepsen et al.*, 2012].

Snow samples were collected for chemical analyses using beveled PVC tubes (50 mm diameter, 500 mm long), which had been soaked in 10% HCl and then rinsed at least five times with deionized water. Duplicate, vertical, contiguous profiles in increments of 40 cm were collected from the snow-air interface to near the snow-ground interface; extreme care was taken to not introduce soil into the lower snow samples. Snow was emptied from the tubes into polyethylene bags (presoaked in 18 MΩ deionized water and dried) and stored at −20°C until analyzed [*Sickman et al.*, 2001]. The depth-integrated concentrations of solutes in

the snowpack for each duplicate core were determined by calculating the volume-weighted mean concentrations (VWM) as in *Williams and Melack* [1991a].

3.2. Surface Water

Discharge from the TOK and GLV4 watersheds was computed from hourly records of stage measured with pressure transducers and rating curves developed from current meter measurements and dye-dilution gauging. During 2000 and 2002–2007, data were linearly interpolated to approximate daily stream nitrate concentrations; stream chemistry was not available in 2001 in TOK.

3.3. Laboratory Methods

All snow and stream samples were first filtered through a 47 mm Whatman Nuclepore membrane with an effective pore size of 1.0 μm. NO_3^- in waters from GLV4 was analyzed on a Metrohm 761 Compact Ion Chromatograph with detection limit of 0.02 μeq L^{-1} [e.g., *Williams et al*., 2006, 2009]. For TOK, NO_3^- was measured on a DIONEX ion chromatograph employing an AS4A or AS14 separation column and chemically suppressed conductivity detection (detection limit, 0.05 μeq L^{-1}). Both laboratories employed rigorous quality control programs including the analysis of duplicates, standard reference materials, and spike recoveries at a 5% frequency in each analytical run.

4. Modeling Methods

4.1. Snow Water Equivalent Reconstruction Model

We used existing results from the SWE reconstruction study conducted by *Jepsen et al*. [2012] to acquire grids of daily snowmelt for GLV4 and TOK, 1996–2007. Here we provide a general description of the SWE reconstruction approach; further details regarding these analyses can be found in *Jepsen et al*. [2012].

The SWE reconstruction approach uses snow-covered area and meteorological data to sum the melt depth of the energy needed to deplete the snowpack at a particular location by a particular known date. To reconstruct maximum SWE for each grid cell, modeled snowmelt was summed for each grid cell over the period of satellite observed snow cover [*Cline et al*., 1998; *Jepsen et al*., 2012; *Molotch et al*., 2008]. Grids of fractional snow-covered area were estimated from Landsat 5 and 7 imagery, using the Thematic Mapper Snow-Covered Area and Grain Size algorithm (TMSCAG) [*Painter et al*., 2009]. Details on correction for canopy and cloud cover, the number and dates of satellite images, and SWE reconstruction model accuracy are provided in *Jepsen et al*. [2012].

Maximum SWE, SWE_0, was derived from the integration of snowmelt that occurred between the dates of satellite-observed snow disappearance and maximum SWE, such that:

$$SWE_0 = \sum_{j=1}^{n} M_j \tag{1}$$

where M_j is the snowmelt that occurs at time step j, and n is the number of time steps that occur between the dates of maximum SWE and snow disappearance [*Jepsen et al*., 2012]. M_j is approximated from

$$M_j = M_{p,j} SCA_j \tag{2}$$

where $M_{p,j}$ is an increment in potential snowmelt at time step j assuming that 100% of the grid cell is snow covered, and SCA_j is the fractional snow-covered area of the grid cell at time step j [*Jepsen et al*., 2012; *Molotch*, 2009]. $M_{p,j}$ is derived from

$$M_{p,j} = E_{p,j} (\rho_w L_f)^{-1} t_{sph} \tag{3a}$$

and

$$E_{p,j} = \max\left[0, min\left[\left(\sum_{k=0}^{j} Q_{net,k}\right), Q_{net,j}\right]\right] \tag{3b}$$

where $E_{p,j}$ is the energy available for snowmelt with respect to the cold content of the snowpack, ρ_w is the density of liquid water, L_f is the latent heat of fusion (3.34×10^5 J kg^{-1}), t_{sph} is 3600 s/h, and $Q_{net,jk,}$ is the

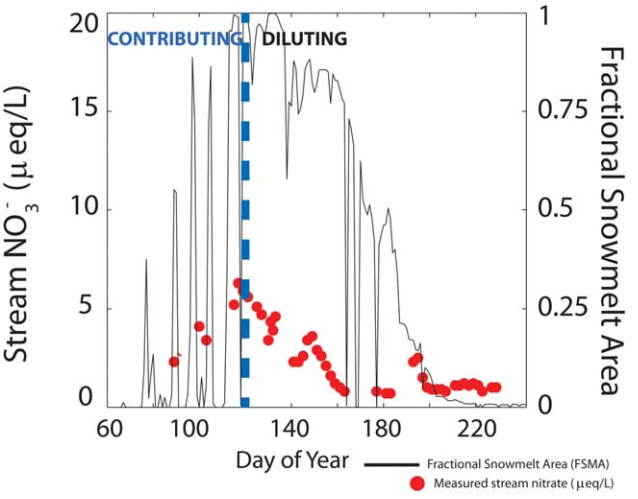

Figure 2. Example time series (TOK 1996) of stream NO_3^- concentration and modeled fractional snowmelt area (FSMA); the blue dotted line illustrates a theoretical point at which pixels may transition from contributing to diluting stream NO_3^-.

net energy flux (W m^{-2}) to the snow surface during time step k or j [*Jepsen et al*., 2012]. $Q_{net,j}$ was calculated by

$$Q_{net,j} = (1-\alpha_{snow})K_j + L_j + Q_{H,j} + Q_{L,j} \quad (3c)$$

where α_{snow} is the albedo of snow, K_j is incident shortwave radiation, L_j is net longwave radiative flux, $Q_{H,j}$ is the sensible heat flux, and $Q_{L,j}$ is the latent heat flux. Each energy flux term was derived following *Jepsen et al*. [2012] using observed forcings interpolated over each basin at 30 m resolution. For a detailed description of the calculation of the cold content and other model components and forcings, see *Jepsen et al*. [2012].

4.2. Defining New Snowmelt Area (NSA)

Locations within a watershed have the potential to contribute NO_3^- to streams if: (i) there is active snowmelt in that area and (ii) there is NO_3^- in the snowpack and/or the soil that can be mobilized by meltwater. It is implicit that there may be varying time scales associated with the response of stream NO_3^- concentrations to snowmelt due to flow path length and complexity related to spatial heterogeneity of hydraulic gradient, slope, and catchment size. Consistent with the VSA concept, we placed emphasis on identifying empirical relationships between the spatiotemporal distribution of grid cells undergoing the early phases of snowmelt (i.e., new snowmelt areas—NSAs) and stream NO_3^- concentration. NSAs produce NO_3^- through preferential elution of snowpack NO_3^- and/or flushing of microbially produced NO_3^- in soils [*Sickman et al*., 2003a]. Grid cells were considered to be NSAs if the amount of seasonal snowmelt for the grid cell remained below a given threshold; we assumed that the amount of NO_3^- that could be eluted from the snowpack or flushed from soils was finite so that grid cells could be depleted in NO_3^- over time. The fraction of the basin classified as new snowmelt area (units: fraction of total basin area) was then used as the explanatory variable with regard to stream NO_3^- concentration.

To identify the optimal method for defining NSAs, and therefore elucidate mechanisms underlying catchment NO_3^- flushing, we conducted a series of regression analyses where NSA was defined in different ways based on time since melting began and cumulative melt volume. After a specified duration or volume of snowmelt was exceeded, the pixel was assumed to be flushed of all NO_3^-, although it could still contribute water to streamflow resulting in solute dilution in the stream (Figure 2). Hence, our approach not only identifies the correlation between the spatiotemporal distribution of snowmelt and stream NO_3^- concentration but it also identifies thresholds which yield the highest correlations. Knowledge of these thresholds are informative with regard to understanding the magnitude and duration of snowmelt required for NO_3^- flushing and for improving hydrochemical model structure.

We estimated NSA in three different ways (abbreviated in Table 2):

NSA definition A: Melt duration. For this definition, pixels were considered new snowmelt areas if the number of days a pixel has been melting was below a specified threshold number of days. We set three "melt-day" (MD) thresholds: 3 days (NSA-MD3), 7 days (NSA-MD7), and 10 days (NSA-MD10). A pixel was considered to be contributing NO_3^- (from the snowpack and soils) from the time it first began melting until it exceeded the allowed number of melt-days (i.e., 3, 7, or 10 days), when mobile NO_3^- was depleted. This definition was based on the hypothesis that it may take a certain amount of time for solutes to travel from the snowpack and soils to the stream and that this time is largely independent of the magnitude of the snow accumulation at any location.

NSA definition B: Percent melt. For this definition, pixels were designated as NSA up until a certain percentage of maximum SWE had melted in an individual pixel. This definition was based on the preferential

Table 2. New Snowmelt Area (NSA) Definitions[a]

Definition	Characterization of Flushing Snowpack (per pixel)
NSA-MD3	Pixel has been melting for up to 3 days
NSA-MD7	Pixel has been melting for up to 7 days
NSA-MD10	Pixel has been melting for up to 10 days
NSA-PM20	Pixel SWE $\leq$ 20% melt loss of initial maximum SWE
NSA-PM35	Pixel SWE $\leq$ 35% melt loss of initial maximum SWE
NSA-PM50	Pixel SWE $\leq$ 50% melt loss of initial maximum SWE
NSA-SD10	Pixel SWE $\leq$ initial maximum SWE $-$ 10 cm SWE
NSA-SD20	Pixel SWE $\leq$ initial maximum SWE $-$ 20 cm SWE
NSA-SD30	Pixel SWE $\leq$ initial maximum SWE $-$ 30 cm SWE

[a]Note that in order for a pixel to be included in the NSA, it must be actively melting. Pixels were not counted as NSA for a particular day if they were not experiencing melt.

elution phenomenon observed for NO_3^- in snowpacks [*Johannessen and Henriksen*, 1978]. We set these percent-melt (PM) thresholds at 20% (NSA-PM20), 35% (NSA-PM35), and 50% (NSA-PM50). Note that this definition results in variability in the specific amount of melt required to flush a pixel, as the percent loss is a function of the maximum SWE per pixel, which varies spatially.

NSA definition C: Specific melt depth. For this definition, pixels contributed NO_3^- until a specific depth (SD) of melt occurred. These specific-depth thresholds were set at 10 cm (NSA-SD10), 20 cm (NSA-SD20), and 30 cm (NSA-SD30) of snowmelt. This NSA definition is based on the hypothesis that a specific amount of water is needed to saturate the soil surface and initiate runoff, consistent with the VSA concept for water and solutes.

There is some error associated with the model such that on any given day a grid cell may have experienced virtually no melt but the modeled estimate of snowmelt may be marginally greater than zero. We have provided a sensitivity analysis of fractional snowmelt area (FSMA) to grid cell melt thresholds of 1 and 5 mm d^{-1} in Appendix A. Grid cells were resultantly defined as melting if modeled snowmelt was greater than 5 mm d^{-1}. FSMA was computed as the sum of all melting cells as a fraction of total basin cells.

A pixel was considered "flushed" of nitrate on the day of year (DOY) it exceeded the NSA threshold (as set in the NSA definitions described above); in other words, this is the date that a pixel theoretically transitions from contributing to diluting stream nitrate. This date will henceforth be referred to as an "index of pixel flushing" (IPF, day of year), which is an index that represents the timing of flushing which can be explored in the context of spatiotemporal variability.

5. Results

5.1. Snow Accumulation and Streamflow

As shown in Figure 3a, GLV4 and TOK exhibited substantial variability in maximum modeled SWE (0.47–1.17 m, 0.68–1.72 m, respectively), suggesting the potential for considerable differences in nitrate flushing behavior over the record analyzed. Both catchments exhibited similar interannual variability in maximum SWE, with coefficients of variation of 0.25 and 0.26 for GLV4 and TOK, respectively. Cumulative seasonal runoff in TOK (during snowmelt season and summer) was more variable for TOK (0.18–1.57 m) than GLV4 (0.54–0.92 m), with greater interannual variability in TOK than GLV4 (CV values of 0.13 and 0.41 for GLV4 and TOK, respectively; see Figure 3b, top plot). Average peak runoff (i.e., basin area normalized discharge) in TOK was 0.024 and 0.020 m/d for GLV4 (Figure 3b, bottom plot). However, peak runoff was approximately 1.6 times more variable in TOK (CV of 0.52) than GLV4 (CV of 0.31).

The average NO_3^- concentration measured in the snowpack at maximum SWE accumulation in GLV4 for all years of measurement was 7.9 μeq L^{-1}, approximately 3.6 times that of the mean value in the TOK of 2.2 μeq L^{-1} (Figure 3c). TOK exhibited greater relative variability in snowpack NO_3^- concentration with a CV of 0.52 versus 0.17 for GLV4. The average peak stream NO_3^- concentration in GLV4, 31 μeq L^{-1}, was almost 4 times greater than the average in TOK, 8.0 μeq L^{-1} (Figure 3d). TOK exhibited relatively greater interannual variability in peak stream NO_3^- concentrations with a CV of 0.63 versus 0.18 for GLV4. The peak stream NO_3^- concentration in TOK occurred 45 days earlier than GLV4 on average. Peak NO_3^- concentration timing was also more variable in TOK versus GLV4 with standard deviations of 55 days and 10 days, respectively.

5.2. Stream NO_3^- Response to Spatially Distributed Snowmelt

In general, expansion and contraction of snowmelt area occurred in TOK during the months of March and April until the entire basin was melting simultaneously in May (Figure 4). In GLV4, FSMA generally oscillated and there were only a few instances where the entire basin was melting simultaneously. The greater

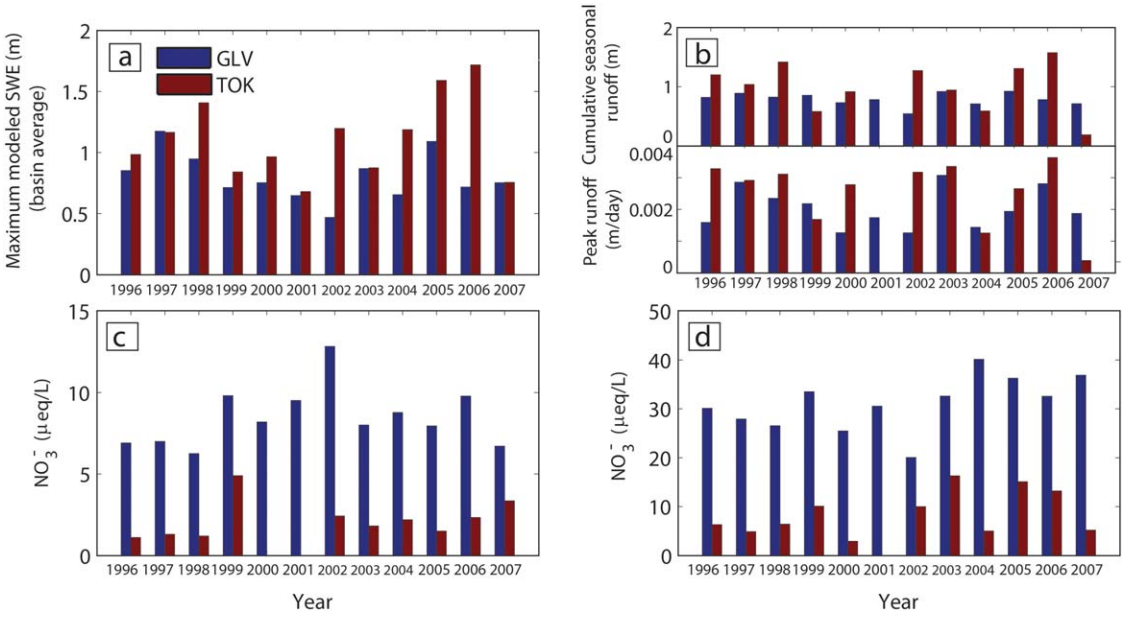

Figure 3. (a) Basin-average maximum SWE values (from SWE reconstruction), (b) cumulative (top plot) seasonal runoff and (bottom plot) peak runoff, (c) basin-average peak snow NO_3^- concentrations, and (d) peak stream NO_3^- concentrations for GLV (blue) and TOK (red).

variability in FSMA at GLV4 may be the result of colder spring-time temperatures at GLV4 and/or the greater spatial variability in snow distribution relative to TOK [*Jepsen et al.*, 2012].

Log-linear regressions of stream NO_3^- concentrations (response variable) and the nine NSA definitions (explanatory variables) reveal high correlation in some years (example shown in Figure 5, see Table 3 for summary of results). TOK exhibited relatively greater correlation between NSA and stream NO_3^- concentrations with a

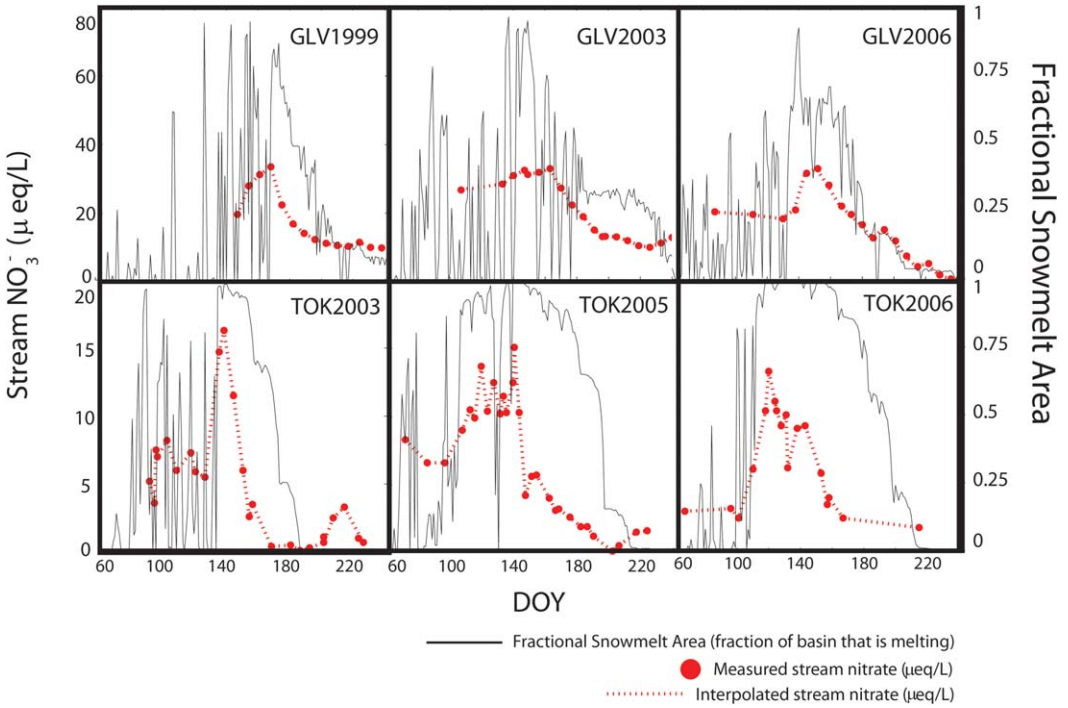

Figure 4. Daily fractional snowmelt area (black) and outflow stream NO_3^- concentrations (red) for (top row) GLV4 and (bottom row) TOK for select representative years between 1996 and 2007; interpolation to daily values are shown with the red dotted line.

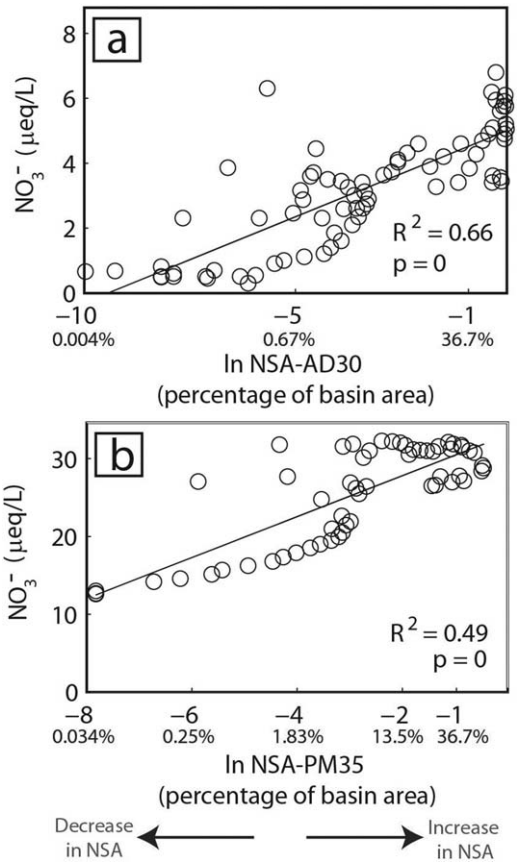

Figure 5. Example plot of New Snowmelt Area (NSA) (horizontal axis) versus stream NO_3^- concentration (vertical axis). Note that the corresponding values for the percentage of basin area are shown below the primary horizontal axis values for ln NSA. Data are shown for (a) TOK in 1996 using NSA-SD30 and (b) GLV4 in 2002 using NSA5-PM35.

mean R^2 of 0.68 for the best fit model of the 12 years versus a mean R^2 of 0.44 for GLV4 (Table 3). The best fit NSA definitions for GLV4 were based on percent mass loss of SWE with NSA-PM50 having the best fit in 5 of 12 years; R^2 values using NSA-PM50 in GLV4 ranged from 0.27 to 0.65 and averaged 0.35. On average, the best fit NSA definitions for TOK were based on specific depth of snowmelt with NSA-SD30 having the best fit in 7 of 11 years, although the goodness of fit for NSA definitions based on percent mass loss were nearly as good. R^2 values using NSA-SD30 in TOK ranged from 0.17 to 0.71 and averaged 0.54. Overall, the NSA definitions based on the number of melt days had the worst fit with observed stream NO_3^- concentrations. In GLV4, 7 of 12 years exhibited an inverse relationship between NSA and stream NO_3^- concentration (1997, 2000, 2002, 2004–2007). In TOK, all 11 years exhibited positive relationships between NSA and stream NO_3^- concentration (1996–2000, 2002–2007). Positive or inverse relationships were not associated with higher or lower R^2 values. In GLV4, other NSA definitions exhibiting strong correlation for particular years were NSA-MD7 (1997), NSA-PM20 (2004, 2005, 2007), and NSA-SD10 (1996, 2000, 2006). In TOK, NSA-PM35 (2005), NSA-PM50 (1999), and NSA-SD20 (2000) exhibited the highest correlation for the respective years.

Based on these results, we defined IPF (index of pixel flushing) for GLV4 as when 50% of the maximum grid cell SWE had melted (NSA-PM50). In GLV4, areas with lower SWE were likely to flush earlier than areas with greater SWE given that the definition of IPF in GLV4 is based on melt reaching 50% of maximum SWE. Wind redistribution of snow within GLV4 is the main determinant of maximum SWE in a pixel [*Erickson et al*., 2005]. The spatial distribution of IPF appears to reflect patterns of wind scour and deposition (Figure 6); e.g., wind scoured areas along ridge lines were flushed earlier than the lower-elevation areas in the valley bottom. These patterns in IPF may also reflect gradients in solar irradiance, with increased snowmelt in areas with greater sky view and south-facing aspects (see supporting information for IPF maps of GLV4 using NSA-SD30 for comparison with TOK using same NSA model).

In contrast to GLV4, for TOK, we defined IPF as when 30 cm of SWE had been lost because NSA-SD30 was the best fit model for the majority of years. The spatial distribution of IPF in TOK, which is based on a specific depth of snowmelt, followed gradients in elevation and aspect associated with the spatial distribution of snowmelt (Figure 6); lower elevation, south and west-facing slopes generally flushed before higher elevation, north or east-facing slopes. GLV4 exhibited greater variability in IPF for the different land cover types relative to TOK (Figure 7, top). In GLV4, the IPF for rock occurred 10 days earlier than talus and 13 days earlier than soil; in TOK, land cover types had no statistically significant effect on IPF (Figure 7, bottom).

5.3. Stream Discharge: Response to Spatially Distributed Snowmelt and Influence on Stream NO_3^-

As a secondary analysis, we also compared spatially distributed snowmelt to stream discharge. Log-linear regressions of discharge (response variable) and the nine NSA definitions (explanatory variables) exhibited similar results to that of the stream NO_3^- concentration-NSA regression analysis. TOK exhibited relatively greater correlation between NSA and discharge with a mean R^2 of 0.51 for the best fit model of the 12 years versus a mean R^2 of 0.29 for GLV4 (Table 4). Both R^2 values were less than that of the stream NO_3^-

Table 3. R^2 Values for Regressions Relating New Snowmelt Area (NSA) Definitions and Stream Nitrate Concentrations for GLV4 (Shaded Rows) and TOK, 1996–2007[a]

NSA	1996	1997	1998	1999	2000	2001	2002	2003	2004	2005	2006	2007
MD3	0.04	**0.45**	0.20	0.17	0.05	0.06	0.25	0.51	0.07	0.00	0.09	0.04
	0.34	**0.47**	0.14	0.13	0.00		**0.21**	0.18	**0.19**	0.09	**0.22**	0.08
MD7	0.08	**0.72**	0.00	0.12	**0.47**	**0.19**	0.04	0.02	**0.28**	0.01	**0.12**	0.03
	0.01	**0.34**	0.01	**0.26**	0.26		**0.27**	0.07	**0.30**	0.03	0.03	0.01
MD10	0.05	**0.37**	0.01	**0.21**	**0.28**	0.02	0.02	0.01	0.01	**0.08**	**0.22**	0.08
	0.30	**0.37**	0.00	**0.39**	**0.35**		**0.43**	**0.17**	**0.27**	**0.10**	**0.00**	0.00
PM20	**0.14**	**0.25**	0.07	0.05	0.06	0.02	0.03	**0.15**	**0.52**	**0.41**	**0.24**	**0.24**
	0.26	**0.53**	**0.06**	**0.39**	**0.23**		**0.47**	0.03	**0.08**	**0.41**	**0.09**	**0.12**
PM35	0.02	0.04	**0.10**	0.21	0.08	**0.37**	**0.21**	**0.49**	0.01	**0.06**	**0.14**	0.02
	0.57	**0.54**	**0.19**	**0.62**	**0.17**		**0.59**	**0.38**	**0.44**	**0.68**	**0.50**	0.00
PM50	**0.06**	**0.39**	**0.27**	**0.31**	**0.49**	**0.51**	**0.35**	**0.65**	**0.04**	**0.07**	**0.09**	**0.03**
	0.60	**0.57**	**0.19**	**0.69**	**0.23**		**0.72**	**0.55**	**0.47**	**0.65**	**0.77**	**0.14**
SD10	**0.16**	**0.40**	0.01	**0.28**	**0.55**	0.08	0.06	0.00	**0.19**	0.05	**0.29**	**0.13**
	0.09	**0.43**	0.00	0.05	**0.33**		**0.29**	**0.08**	**0.24**	0.02	**0.01**	0.01
SD20	0.06	**0.13**	**0.11**	**0.29**	0.11	0.10	0.05	0.00	0.05	**0.27**	**0.23**	**0.11**
	0.59	**0.60**	**0.10**	**0.63**	**0.34**		**0.69**	**0.23**	**0.59**	**0.25**	**0.11**	0.04
SD30	0.00	0.00	**0.14**	**0.22**	0.03	**0.46**	**0.15**	**0.34**	**0.07**	**0.10**	**0.14**	0.01
	0.66	**0.71**	**0.34**	**0.68**	**0.29**		**0.76**	**0.56**	**0.70**	**0.62**	**0.37**	**0.16**
Max R^2	0.16	0.72	0.27	0.31	0.55	0.51	0.35	0.65	0.52	0.41	0.29	0.24
	0.66	0.72	0.34	0.69	0.55	N/A	0.76	0.65	0.70	0.65	0.77	0.24
Best NSA	SD10	MD7	PM50	PM50	SD10	PM50	PM50	PM50	PM20	PM20	SD10	PM20
	SD30	SD30	SD30	PM50	SD20	N/A	SD30	SD30	SD30	PM35	PM50	SD30
+ or – corr.	+	–	+	+	–	+	–	+	–	–	–	–
	+	+	+	+	+	N/A	+	+	+	+	+	+

[a]The maximum R^2 value, best fit NSA definition, and signage of best fit correlation for each year are shown in the last six rows. Values that are statistically significant at the 95% confidence level are set in bold.

concentration-NSA regression analysis; this is likely because the stream discharge values vary with summer rains while the snowpack has mostly disappeared and snowmelt declined. The best fit NSA definitions for GLV4 were largely based on specific-depth melt loss of SWE, with NSA-SD20 and NSA-SD30 having the best fit in a combined 5 of 12 years; R^2 values using NSA-SD20 in GLV4 ranged from 0 to 0.5, with a mean of 0.22. On average, TOK showed the best fit NSA definitions based on specific-depth melt loss of SWE as well, with NSA-SD30 having the best fit in 4 of 12 years (SD10, SD20, and SD30 in all accounted for the best fit NSA definitions in 8 of 11 years). R^2 values using NSA-SD30 in TOK ranged from 0.11 to 0.62 and averaged 0.42.

We also compared stream discharge and stream NO_3^- concentrations for GLV4 and TOK. Generally, GLV4 exhibited a stronger relationship between stream discharge (explanatory variable) and stream NO_3^- concentration (response variable) (Figure 8), with R^2 values ranging from linear regressions ranging from 0.02 to 0.72 and averaging 0.2. In TOK, R^2 values ranged from 0 to 0.73, with an average R^2 of 0.13. In TOK, the years 2000 and 2007 produced the only notably high correlation coefficients, with most other years exhibiting very low correlation. This may suggest that nitrate and snowmelt reach the stream at similar times through deeper flow paths in GLV4, but that much of the snowpack and terrestrially flushed nitrate reaches the stream during the first pulse of snowmelt rather than during peak snowmelt in TOK (more in section 6).

5.4. Snowmelt Model Error Influence on NSA Regression Analyses

To assess the effects of error from the SWE reconstruction model on our NSA-regression analyses, we compared model forcing errors summarized in *Jepsen et al.* [2012] to our stream NO_3^- concentration-NSA regression results. Error associated with modeled downward longwave radiation, residuals of air temperature, water vapor pressure, and wind speed, and modeled SWE error values from *Jepsen et al.* [2012] are reproduced below.

5.4.1. Downward Longwave Radiation

Longwave errors were evaluated at two sites in TOK (Emerald Lake, EML and Topaz Lake, TPL) and one site near GLV4 (Subnivian, SUBNIV) from March 1 to August 31 [see *Jepsen et al.*, 2012, Figure 9]. The model bias for TOK downward longwave (1998, 1999, 2003–2007) (model-observed) was −31 W/m^2 (standard deviation of 8.7 W/m^2) and −2.0 W/m^2 (standard deviation of 5.5 W/m^2) for EML and TPL, respectively. The model bias for GLV4 downward longwave (1997–2007) (model-observed) was −23 W/m^2 (SUBNIV). From this, we

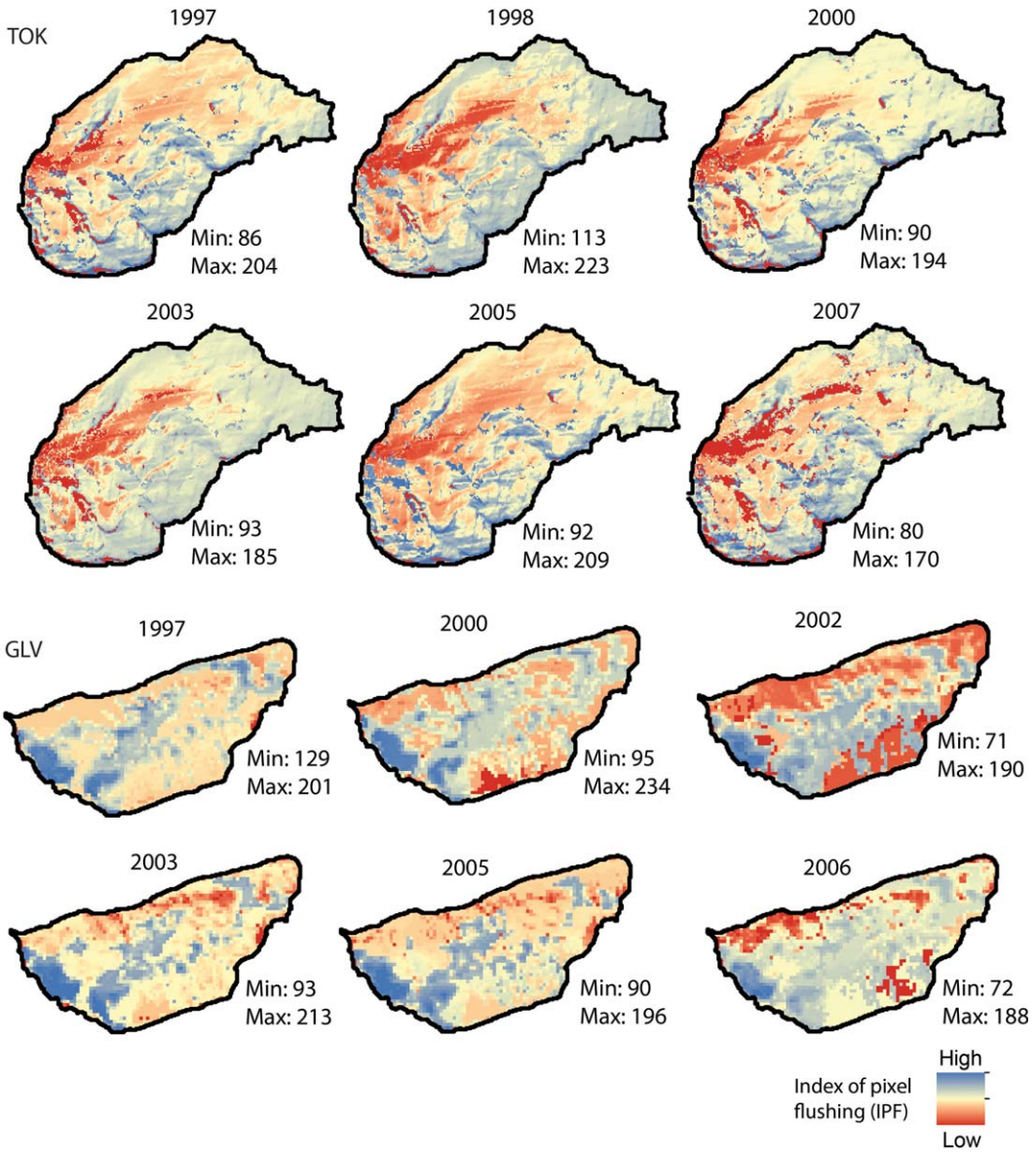

Figure 6. Index of pixel flushing (DOY) for TOK (NSA-SD30) and GLV4 (NSA-PM50) for select representative years between 1996 and 2007. Red indicates the earliest flushing dates and blue indicates the later flushing dates. Note that different scales are used in each map corresponding to the minimum and maximum values indicated.

estimated the amount of melt generated from these biases in longwave radiation. We found a mean melt bias of −8 mm/d at EML (TOK), −0.5 mm/d at TPL (TOK), and −5.9 mm/d at SUBNIV (GLV4). If we perturb these mean biases within 1 standard deviation of the mean, we produce melt bias ranges of −10.3 to −5.8 mm/d for EML (TOK), −1.9 to 0.9 mm/d for TPL (TOK), and −8.1 to −3.8 mm/d for SUBNIV (GLV4). The observations at the EML site in TOK appear to be drifting upward in value with time [*Jepsen et al*., 2012, Figure 8, upper right]; this seems peculiar and may represent increasing observation errors with time (possibly leading to overestimates in model longwave error). Nonetheless, the model underestimated the downward longwave flux similarly in both GLV4 and TOK, resulting in similar melt biases of −4.25 for TOK (averaging EML and TPL) and −5.9 mm/d for GLV4.

We also evaluated the impact of these biases on NSA-stream nitrate correlation results (Figure 9). We found low correlation coefficients of 0.17, 0.0003, and 0.11 for SUBNIV (GLV4), EML (TOK), and TPL (TOK), respectively. None of these R^2 values were significant at the $p < 0.05$ level, and thus we found no effective relationship between longwave bias and NSA-stream nitrate correlation.

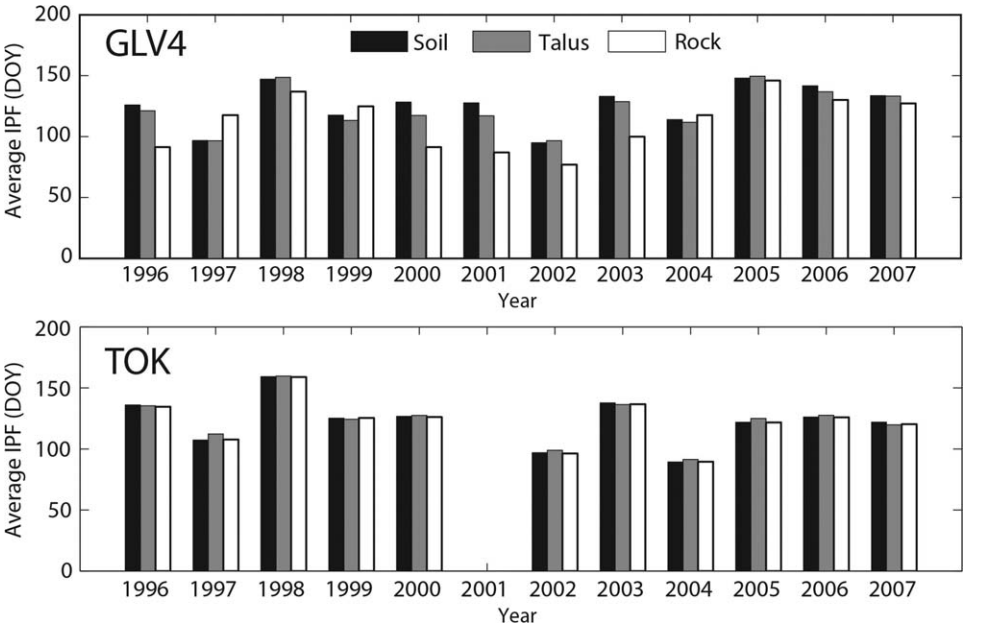

Figure 7. Average Index of Pixel Flushing (IPF) values for basin subunits in (top) GLV4 and (bottom) TOK.

5.4.2. Air Temperature, Water Vapor Pressure, and Wind Speed

The reduced residuals of the meteorological forcings used in the reconstruction model were calculated to assess potential errors in the interpolated model forcings [see *Jepsen et al*., 2012]. To compute the reduced residuals, observations of air temperature, water vapor pressure, and wind speed at each meteorological station were compared to values computed from a "jackknifing" interpolation method between the other stations [*Molotch*, 2009; *Jepsen et al*., 2012]. We compared the reduced residuals from the meteorological

Table 4. R^2 Values for Regressions Relating New Snowmelt Area (NSA) Definitions and Stream Discharge for GLV4 (Shaded Rows) and TOK, 1996–2007[a]

NSA	1996	1997	1998	1999	2000	2001	2002	2003	2004	2005	2006	2007
MD3	0.01	**0.41**	**0.06**	**0.11**	**0.07**	0.01	0.00	0.02	0.00	0.02	**0.47**	**0.25**
	0.26	**0.47**	0.01	**0.65**	**0.59**		**0.45**	**0.17**	**0.79**	**0.06**	**0.10**	**0.80**
MD7	**0.24**	**0.40**	**0.12**	**0.14**	**0.13**	0.00	0.02	0.03	0.02	**0.09**	**0.47**	**0.17**
	0.32	**0.53**	**0.02**	**0.65**	**0.69**		**0.59**	**0.22**	**0.77**	**0.19**	**0.12**	**0.75**
MD10	**0.36**	**0.41**	**0.04**	**0.14**	**0.17**	0.00	**0.04**	**0.37**	**0.07**	**0.12**	**0.49**	**0.21**
	0.29	**0.52**	0.02	**0.61**	**0.68**		**0.67**	**0.26**	**0.74**	**0.19**	**0.16**	**0.77**
PM20	0.01	**0.41**	0.01	**0.18**	**0.17**	0.00	**0.05**	**0.09**	0.01	**0.08**	**0.45**	**0.18**
	0.18	**0.34**	0.01	**0.50**	**0.54**		**0.50**	**0.18**	**0.66**	**0.14**	**0.05**	**0.67**
PM35	**0.12**	**0.41**	**0.06**	**0.22**	**0.23**	**0.05**	**0.12**	**0.32**	**0.09**	**0.22**	**0.49**	0.00
	0.26	**0.44**	0.00	**0.48**	**0.57**		**0.57**	**0.23**	**0.76**	**0.20**	**0.09**	**0.69**
PM50	**0.20**	**0.15**	**0.09**	**0.23**	**0.27**	**0.20**	**0.15**	**0.30**	**0.14**	**0.37**	**0.44**	**0.11**
	0.19	**0.34**	0.00	**0.39**	**0.52**		**0.52**	**0.26**	**0.79**	**0.20**	**0.15**	**0.72**
SD10	0.01	**0.40**	**0.07**	**0.15**	**0.14**	0.00	0.03	0.03	0.02	**0.11**	**0.47**	**0.19**
	0.30	**0.56**	0.00	**0.56**	**0.63**		**0.57**	**0.28**	**0.79**	**0.13**	**0.10**	**0.78**
SD20	**0.32**	**0.44**	**0.10**	**0.24**	**0.24**	0.00	**0.06**	**0.38**	**0.10**	**0.13**	**0.50**	**0.16**
	0.35	**0.56**	**0.06**	**0.55**	**0.67**		**0.67**	**0.27**	**0.69**	**0.27**	**0.26**	**0.63**
SD30	**0.28**	**0.20**	0.00	**0.25**	**0.28**	**0.07**	**0.09**	**0.28**	**0.25**	**0.17**	**0.48**	0.00
	0.28	**0.32**	**0.11**	**0.42**	**0.59**		**0.59**	**0.37**	**0.62**	**0.42**	**0.32**	**0.58**
Max R^2	0.36	0.44	0.12	0.25	0.28	0.20	0.15	0.38	0.25	0.37	0.50	0.25
	0.35	0.56	0.11	0.65	0.69	N/A	0.67	0.37	0.79	0.42	0.32	0.80
Best fit NSA	MD10	SD20	MD7	SD30	SD30	PM50	PM50	SD20	SD30	PM50	SD20	MD3
	SD20	SD10	SD30	MD7	MD7	N/A	SD20	SD30	SD10	SD30	SD30	MD3

[a]The maximum R^2 value and best fit NSA definition for each year are shown in the bottom rows. Values that are statistically significant at the 95% confidence level are set in bold.

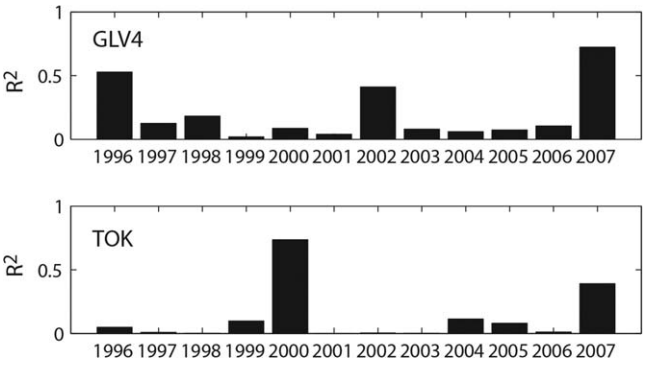

Figure 8. R^2 values for stream discharge-stream NO_3^- concentration correlation, 1996–2007 ((top) GLV4; (bottom) TOK).

stations [*Jepsen et al.*, 2012, Table 4] to our best fit R^2 values from the NSA-nitrate correlation analyses (Figure 10). We did not find significant relationships between residuals and NSA-nitrate correlation coefficients (all p values > 0.05).

5.4.3. Spatially Distributed SWE

We compared basin-average modeled maximum SWE error (modeled-measured/measured, %) [see *Jepsen et al.*, 2012, Figure 5] to the best fit R^2 value from the NSA-stream nitrate correlation analyses for each year (Figure 11). For both TOK and GLV4, there does not appear to be a significant relationship between model error and R^2 values from the NSA-nitrate correlation ($p > 0.05$). Furthermore, the average absolute model error as a percent of observed SWE was 16% for TOK and 17% for GLV4. Despite this similarity in snowmelt model performance, there were large differences in NSA-stream nitrate correlation between the two basins (average R^2 values of 0.68 for TOK and 0.44 for GLV4).

6. Discussion

6.1. NO_3^- and New Snowmelt Area Relationships

Our overarching questions were whether spatiotemporal patterns in snowmelt explain temporal patterns of NO_3^- in streams, and whether this differed between basins. In TOK, the relationship between NSA indices and the stream NO_3^- patterns were fairly consistent from year to year and showed: (i) that NO_3^- concentrations tended to increase when NSA was expanding and (ii) NO_3^- concentrations declined sharply once the IPF threshold was crossed and the entire catchment was melting (Figure 4). For all years of analysis in TOK (1996–2000, 2002–2007), there was a positive correlation between the NSA indices and the stream NO_3^- concentration. Furthermore, the NSA based on accumulated depth of snowmelt explained as much as 76% of the variability in stream NO_3^- concentration in some years (Table 3). These observations demonstrate strong hydrologic connectivity between hillslopes and streams within TOK as the variability in the stream NO_3^- was related to the variability in the timing and distribution of snowmelt, which is consistent with the VSA hypothesis and the fact that the TOK lacks a large reservoir of groundwater. Additionally, the best-correlated definition of NSA in TOK was NSA-SD30, suggesting that stream NO_3^- chemistry is sensitive not only to changes in the distribution and timing of snowmelt, but also to changes in the magnitude of snowmelt. Based on mass balance studies from seven high-elevation Sierra Nevada catchments, *Sickman et al.* [2001] observed a strong positive relationship between stream NO_3^- concentrations and the depth of the snowpack and duration of

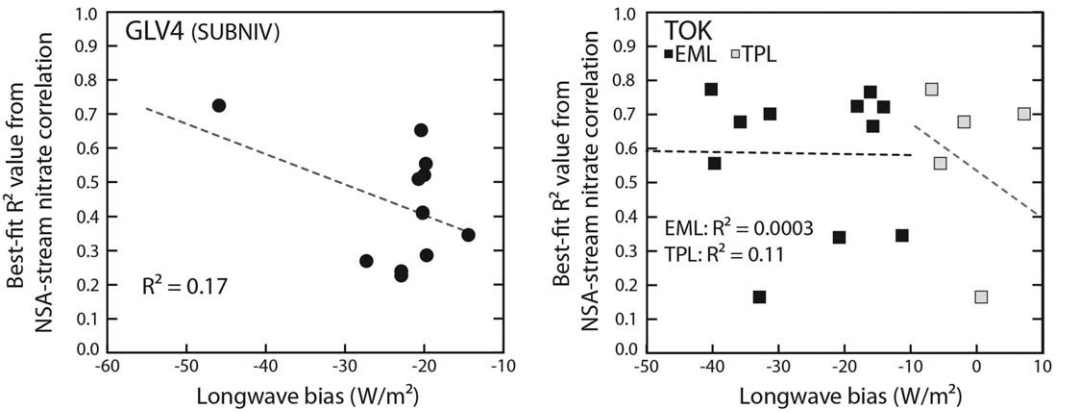

Figure 9. Correlation plots for downward longwave radiation errors and correlation coefficients from NSA-NO_3^- analyses, 1996–2007.

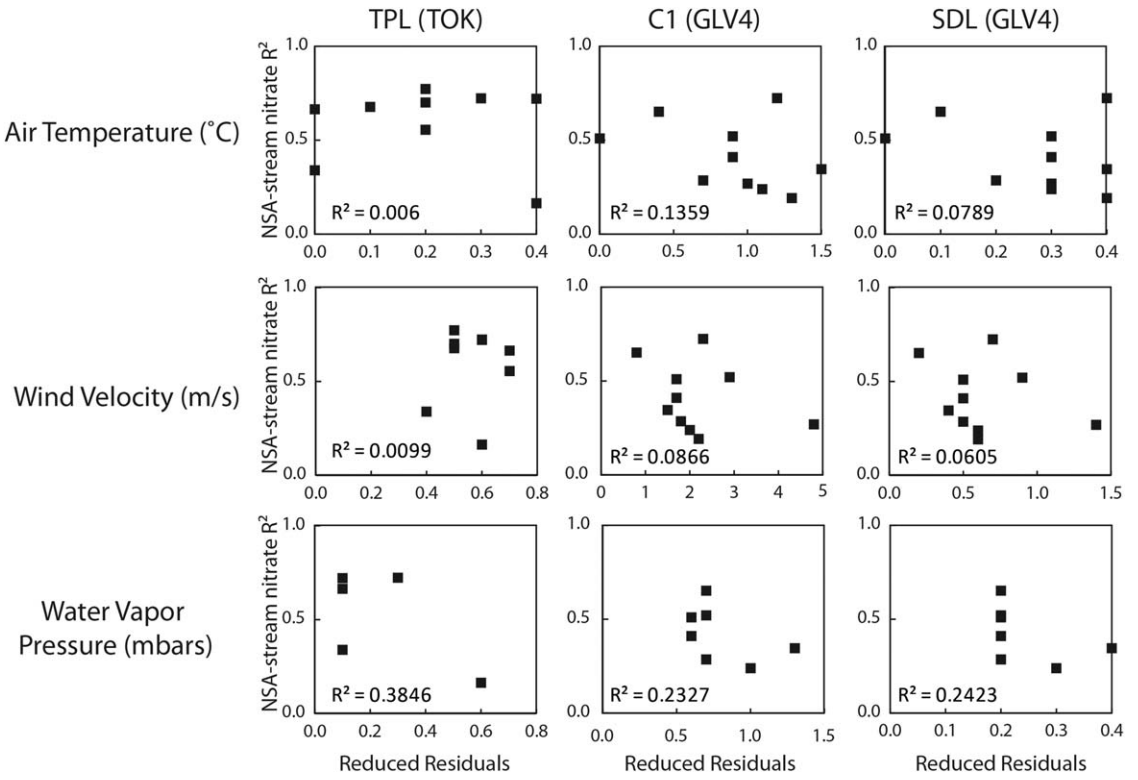

Figure 10. Correlation plots for reduced residuals of air temperature, wind velocity, and water vapor pressure and correlation coefficients from NSA-NO_3^- analyses, 1996–2007.

snow cover. Large snow-years resulted in larger pools of mobile NO_3^- in soils and shorter growing seasons which reduced overall N retention in catchments. These pools of labile soil nitrate are likely extensive in TOK given the fact that the PM50 and SD30 indices were better correlated with NO_3^- than the lower duration/volume indices (Table 3).

In contrast, GLV4 exhibited much more variability in relationships between NSA and stream NO_3^- concentrations than TOK. This could be related to high concentrations of chemical constituents released by glacial processes in GLV4 (more below), or the greater variability in modeled SWE in GLV4 as compared to TOK, largely due to influences of wind redistribution of snow into deep drifted pockets and off ridges and microtopography prone to wind scour [*Jepsen et al.*, 2012]. Significantly, in many years, NO_3^- concentrations did not peak until NSA began to decrease and the IPF threshold for the catchment had been crossed. Substantial differences exist between TOK and GLV4 in N deposition rates, vegetation cover, catchment area, and in

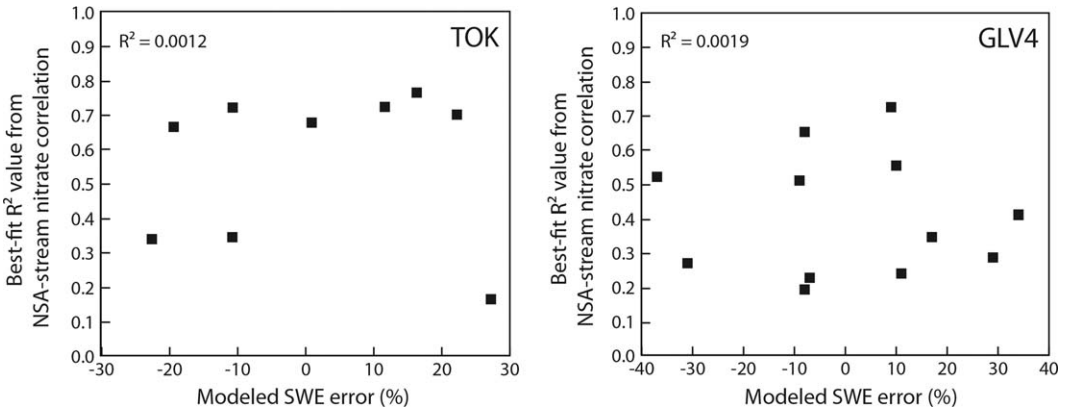

Figure 11. Correlation plots for modeled maximum SWE errors and correlation coefficients from NSA-NO_3^- analyses, 1996–2007.

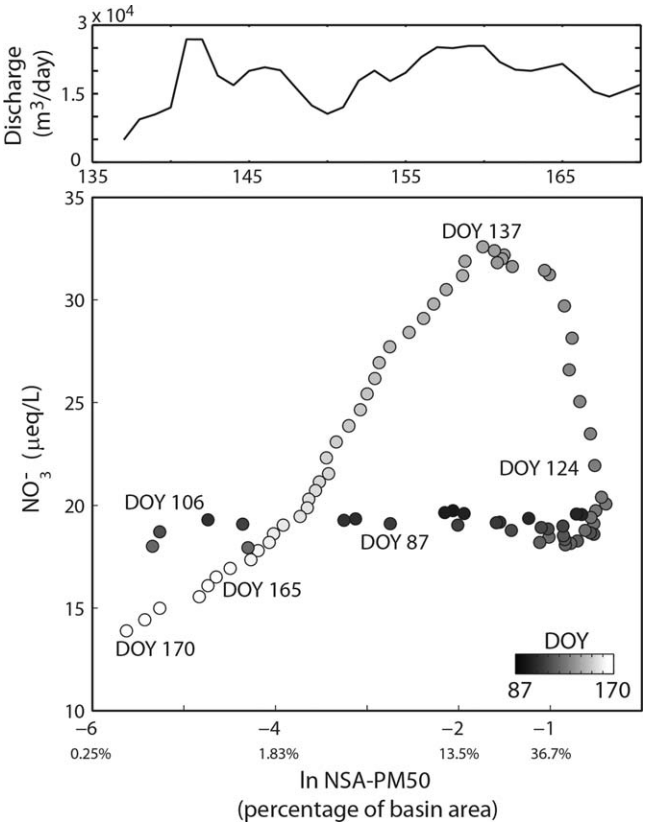

Figure 12. (top) Discharge in GLV4 for 2006, and (bottom) relationship between NSA-PM50 (horizontal axis) and stream NO_3^- concentration in GLV4 for 2006 (the corresponding values for the percentage of basin area are shown below the primary horizontal axis values for ln NSA). Note the counterclockwise hysteresis exhibited by the data.

the timing of snowmelt. However, the relatively poor performance of the NSA indices at GLV4 in predicting patterns of stream NO_3^- suggests that hillslope snowmelt and stream NO_3^- concentrations are relatively decoupled due to deeper flow paths that exist in the basin [*Liu et al.*, 2004; *Molotch et al.*, 2008]. Evidence for this hypothesis includes the counterclockwise hysteresis depicted in Figure 12, which shows that stream NO_3^- concentrations were greater on the receding limb of NSA than on the rising limb. Initially, the stream NO_3^- concentration remained constant while NSA expanded; constancy of NO_3^- while discharge is rising suggests piston-flow displacement of an unconfined aquifer and other water stored in the catchment (e.g., water held in Lakes 4 and 5, Figure 1). By DOY 124, NO_3^- concentration increased rapidly with a slight decrease in NSA, which likely indicates a transition toward a greater proportion of surface flow (unreacted snowmelt), shallow throughflow in saturated soils, and water draining talus regions [*Liu et al.*, 2004]. Subsequently, decreases in NSA around DOY 137 resulted in decreased NO_3^- concentration. This type of counterclockwise hysteresis was not observed in TOK. Counterclockwise (i.e., negative) hysteresis was exhibited in 1996, 1997, 2000, 2003, 2005, and 2006 in GLV4 (for best fit definition, NSA-PM50). The other years (1998, 1999, 2001, 2002, 2004, and 2007) did not exhibit strong hysteresis, but exhibited a decline in stream nitrate concentration concurrent with a decline in NSA. It is important to note that Green Lake 4 (which lies just above the basin outflow) has the potential for storage of chemical constituents, and may have affected these hysteresis curves and our results. Storage and transformation of nitrate in the alpine lakes in TOK and GLV4 should be explored in future research.

The details of these hydrologic processes are beyond the scope of this paper, but we can base a conceptual explanation of the hysteresis on previous works. *Jepsen et al.* [2012] found that streamflow in GLV4 was decoupled from snowmelt, suggesting significant subsurface flow. The findings of *Liu et al.* [2004] also indicate the presence of significant groundwater flow in GLV4 and associated saturation-excess overland flow near stream channels, with no stream response to initial snowmelt, and 64% of old water (talus flow and base flow) accounting for discharge during high flow in GLV4. Our NSA-discharge analysis also supports this, in that there was greater correlation between NSA and discharge in TOK than GLV4 (R^2 values of 0.51 and 0.29, respectively), and that stream nitrate concentration and discharge were on average slightly better correlated in GLV4 compared to TOK (R^2 values of 0.2 and 0.13, respectively). We hypothesize that the hysteresis loops in GLV4 likely resulted from changes in the proportions of old and new water and the degree of hydrologic connectivity within the catchment as snowmelt progressed. For example, prior to DOY 123 in GLV4 in 2006, NSA oscillated while stream NO_3^- concentrations remained constant. During this period, old water with moderate levels of NO_3^- was likely the dominant source of water to streams. From DOY 123 to 130, there is a steady increase in stream NO_3^- concentration with a decrease in the log of NSA, consistent with a shift toward dominance of surface and talus waters which have higher NO_3^- concentrations. Contributing to these changes in source water was the basin's melting pattern, which started at the basin edges over rock subunits, and then progressed inward toward the

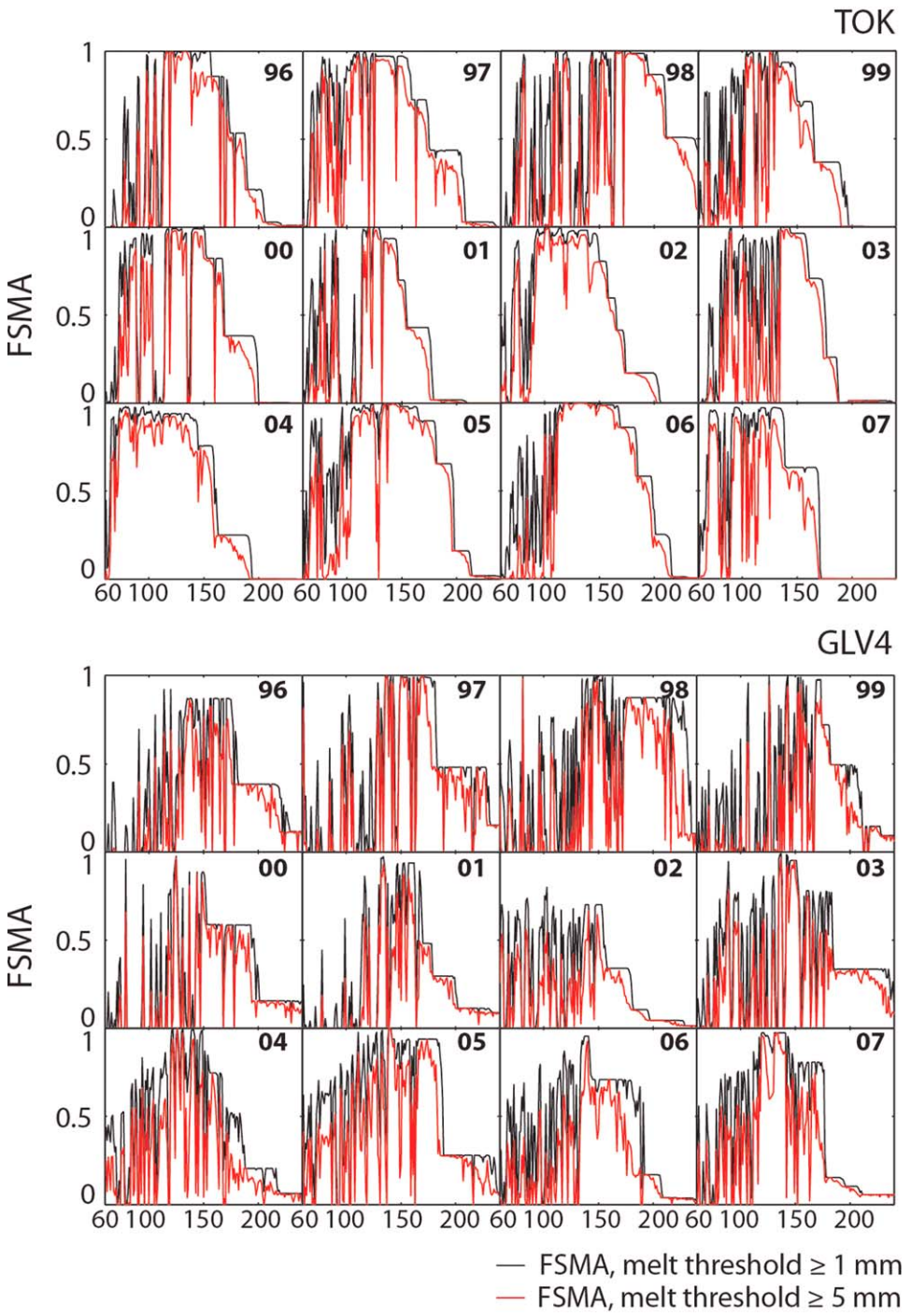

Figure A1. Time series of fractional snowmelt area (FSMA) using grid cell melt thresholds of 1 and 5 mm for (top) TOK and (bottom) GLV4, 1996–2007.

basin outflow over soil and talus subunits, which should contain potentially greater pools of NO_3^- [*Williams et al.*, 1996b, 1997]. It is possible that a certain magnitude of melt is required to initiate surface flow paths. Based on our analyses, as well as previous works [*Liu et al.*, 2004; *Molotch et al.*, 2008; *Williams et al.*, 1997], it is likely that individual basin topography and geology, and snow accumulation and melt patterns result in flow paths that differ substantially between TOK and GLV4. This cause may be important to the differences in stream nitrate response to snowmelt between these two basins. Because TOK and GLV4 are fairly representative of other alpine catchments in the Sierra Nevada and the Rocky Mountains (respectively), it is possible that other basins in these ranges may behave similarly.

6.2. Assumptions and Limitations

Adding to the complexity of NO_3^- concentration patterns is the climate-change induced melting of glaciers and permafrost in the Rocky Mountains [*Baron et al*., 2012; *Saros et al*., 2010]. At GLV4, annual catchment NO_3^- yield increased between 2000 and 2009 despite a decrease in atmospheric deposition of inorganic nitrogen [*Barnes et al*., 2013]. Concurrent increases of silica and base cations over this period suggest that accelerating glacier melt and thawing of alpine permafrost is contributing to rising catchment NO_3^- yields by: (i) increasing hydrologic connectivity between hillslopes and streams during the summer and (ii) mobilizing cryogenically preserved NH_4^+ which is then nitrified and exported from the catchment [*Barnes et al*., 2013]. These processes are most likely to affect stream NO_3^- patterns in the later stages of snowmelt and may be contributing to the counterclockwise hysteresis pattern shown in Figure 12. Glacial features and permafrost are not found in TOK and tend to be rare in the Sierra Nevada.

We also examined the effects of rain-on-snow events in each basin, as these events cause rapid flushing of the snowpack and may have affected our results. We found that for GLV4, 1996 was the sole year for which there was a significant precipitation event at the stream nitrate peak that occurred concurrent to a period of above-zero temperatures. The correlation between NSA and stream nitrate was lowest for this year for GLV4. In TOK, only 1998 and 2005 displayed precipitation events during periods of above-zero temperatures during the stream nitrate peak. The year 1998 did exhibit low correlation ($R^2 < 0.4$), but 2005 had high correlation. It is possible that spring rain events on the snowpack may have influenced our results for those years in GLV4 and perhaps also in TOK.

Several assumptions inherent in the models used in this work may influence the results of this study. In particular, the model used to estimate the spatial distribution of snowmelt has uncertainty in model structure, model parameters, and model forcings. For example, the parameterization of snow-surface albedo in the SWE reconstruction model contains uncertainty associated with the distribution of impurities and variability in the evolution of the snow surface associated with variability in the distribution of snow grain size [*Molotch et al*., 2004; *Molotch and Bales*, 2006]. Parameterization of the snow cover depletion curves introduces uncertainty associated with errors in the satellite observed timing of snow disappearance [*Slater et al*., 2013]. It is important to note that the snow cover retrieval algorithm (TMSCAG) has inherent uncertainties that may limit detection of extremely discontinuous snow, such as snow in talus fields. In addition, the 30 m resolution of the data limits detection of snow patches within a pixel smaller than 15% of the pixel area. Snowfall events after maximum accumulation are not explicitly considered in the model, leading to model structural errors that can influence estimates of SWE; note this error source resulted in less than 10% error in SWE estimates [*Jepsen et al*., 2012]. Furthermore, setting the cold content to zero each night may have resulted in an overestimation of early season melt [*Jepsen et al*., 2012]. This is of particular importance for GLV4, where snowmelt initiation during the spring occurs in fits and starts that is typical of a continental climate and snowpack regime. Measurements of snow temperature and snow density in snow pits in GLV4 indicate that the snowmelt model's relatively crude treatment of cold content may have overestimated early season melt; calculations for nonisothermal snowpacks during 1996–2007 indicate cumulative modeled snowmelt prior to cold content exhaustion ranged from 1 to 11 cm.

Uncertainty in model forcings leads to errors in the SWE reconstruction model; RMSE values for solar radiation were 79 W m^{-2} (TOK) and 75 W m^{-2} (GLV4), and RMSE values for longwave radiation were 28 W m^{-2} (TOK) and 36 W m^{-2} (GLV4). Estimates of solar radiation may be particularly biased during periods of cloud cover [*Slater et al*., 2009]. Estimates of long wave radiation may be particularly uncertain in areas near exposed bedrock, which can be a significant source of longwave radiation to adjacent snow-covered areas [*Molotch et al*., 2004]. Other methods of estimating longwave radiation may have less inherent error than the *Idso* [1981] method used to produce the snowmelt modeling results used in this study from *Jepsen et al*. [2012] [*Flerchinger et al*., 2009]. Despite these sources of uncertainty, estimates of snowmelt used in this research are considered to be of high quality relative to other modeling approaches. We did not find significant impacts of snowmelt model error associated with downward longwave, air temperature, water vapor pressure, wind speed, or modeled maximum SWE on the stream NO_3^- concentration-NSA analyses.

7. Conclusions

The primary goal of this study was to explore the influence of spatiotemporal variability in snowmelt on stream NO_3^- concentration in two geologically and climatologically dissimilar basins. The two watersheds

exhibited significantly different levels of nitrate loading and export with average snowpack nitrate concentrations 3.6 times greater in GLV4 versus TOK and average peak stream nitrate concentrations 3.9 times greater in GLV4. Nitrate export in TOK was strongly influenced by spatiotemporal patterns in snowmelt. Through correlation of stream NO_3^- with various definitions of new snowmelt area (i.e., as a proxy for areas of NO_3^- flushing), we found that on average, the modeled spatial distribution of new snowmelt area (NSA) explained 68% of the variability in the stream NO_3^- concentration in TOK versus 44% in GLV4. The correlations between new snowmelt area and stream NO_3^- concentration were consistently positive in TOK indicating flushing of soil NO_3^- consistent with variable source area regulation of hydrology and nitrogen losses. In GLV4, both positive and negative correlations between NSA indices and NO_3^- patterns were observed. In some years, NO_3^- concentrations were higher on the falling limb of the snowmelt hydrograph which induced a strong counterclockwise hysteresis between NSA and NO_3^- patterns in GLV4. The delayed response of stream NO_3^- concentration with respect to NSA suggests slower and deeper flow paths connect hillslopes to streams in GLV4 relative to TOK. These results have important implications for understanding alpine ecosystem response to climate change as a more rapid onset of spring may lead to a more rapid expansion of nitrate contributing areas, potentially leading to greater peak nitrate concentrations.

The work presented here identified how spatiotemporal snowmelt patterns influence the distribution of nitrate contributing areas under a variety of climatic conditions at two catchments with differing hydrologic architectures. While future climate conditions were not directly assessed, future research could address climate scenarios within this type of analysis to assess impacts on nitrate and other hydrochemical components. As global temperatures rise, the timing of snowmelt could advance by as much as 6 weeks [*Adam et al.*, 2009; *Clow*, 2010; *Magnusson et al.*, 2010; *Mote*, 2006]. It is hypothesized that warmer spring/early summer air temperatures will likely increase the relative importance of thermal radiation and sensible heat flux with respect to snowmelt. Hence, warmer spring air temperatures will likely lead to more rapid expansion of nitrate contributing area as the distribution of thermal radiation and turbulent fluxes are more uniformly distributed across alpine watersheds relative to solar radiation. This more rapid expansion of nitrate contributing area may lead to greater peak nitrate concentrations in surface water-dominated systems such as TOK; however, this effect could be mitigated by greater microbial N demand in warmer soils and greater plant growth. The potential impacts of regional warming on nitrate concentrations in GLV4 are even less clear as regional warming will also result in increased ecosystem N demand owing to expansion of the plant growing season, earlier ice-off in lakes, increased glacial melt, and thawing permafrost; all of which add additional complexity to interactions among climate, atmospheric deposition and hydrology in high-elevation catchments.

Appendix A: Melt Thresholds for Determining Fractional Snowmelt Area

We compared fractional snowmelt area (FSMA) using melt thresholds of 1 and 5 mm (Figure A1). Grid cells were considered melting only when they were equal to or exceeded the melt threshold. In TOK, $FSMA_{melt\ \geq 1\ mm}$ exceeded $FSMA_{melt\ \geq 5\ mm}$ by as much as 86% of the basin area for 1996–2007. In GLV4, $FSMA_{melt\ \geq 1\ mm}$ exceeded $FSMA_{melt\ \geq 5\ mm}$ by as much as 68% of the basin area for 1996–2007. For our study, we chose to define grid cells as melting if modeled snowmelt was greater than 5 mm d^{-1}, as there is some error associated with the model such that on any given day a grid cell may have experienced virtually no melt but the modeled estimate of snowmelt may be marginally greater than zero (e.g., 0.05 mm d^{-1}).

Acknowledgments
This project was funded by NSF Hydrological Sciences grants EAR1032295 and EAR1032308, the NSF-funded Niwot Ridge Long-Term Ecological Research project, and NSF's Boulder Creek Critical Zone Observatory. Many thanks to Suzanne Anderson, Nel Caine, Galen McLauren, Michael Gleason, and Leah Meromy. Data can be obtained from http://niwot.colorado.edu/ and http://ccb.ucr.edu/emeraldlake/.

References

Adam, J. C., A. F. Hamlet, and D. P. Lettenmaier (2009), Implications of global climate change for snowmelt hydrology in the twenty-first century, *Hydrol. Processes*, *23*, 962–972.

Bales, R. C., R. E. Davis, and D. A. Stanley (1989), Ion elution through shallow homogeneous snow, *Water Resour. Res.*, *25*, 1869–1877.

Barnes, R. T., M. W. Williams, J. N. Parman, K. Hill, and N. Caine (2013), Thawing glacial and permafrost features contribute to nitrogen export from Green Lakes Valley, Colorado Front Range, USA, *Biogeochemistry*, *117*, 413–430, doi:10.1007/s10533-013-9886-5.

Baron, J. S., E. K. Hall, B. T. Nolan, J. C. Finlay, E. S. Bernhardt, J. Harrison, F. Chan, and E. W. Boyer (2012), The interactive effects of excess reactive nitrogen and climate change on aquatic ecosystems and water resources of the United States, *Biogeochemistry*, *114*(1–3), 71–92.

Brooks, P. D., and M. W. Williams (1999), Snowpack controls on nitrogen cycling and export in seasonally snow-covered catchments, *Hydrol. Processes*, *13*, 2177–2190.

Burns, D. A. (2003), Atmospheric nitrogen deposition in the Rocky Mountains of Colorado and southern Wyoming—A review and new analysis of past study results, *Atmos. Environ.*, *37*, 921–932.

Caine, N. (1995), Temporal trends in the quality of streamwater in an alpine environment: Green Lakes Valley, Colorado Front Range, USA, *Geogr. Ann., Ser. A*, *77*, 207–220.

Campbell, D. H., C. Kendall, C. C. Y. Chang, S. R. Silva, and K. A. Tonnessen (2002), Pathways for nitrate release from an alpine watershed: Determination using δ^{15}N and δ^{18}O, *Water Resour. Res.*, *38*(5), doi:10.1029/2001WR000294.
Cline, D. W., R. C. Bales, and J. Dozier (1998), Estimating the spatial distribution of snow in mountain basins using remote sensing and energy balance modeling, *Water Resour. Res.*, *34*, 1275–1285.
Clow, D. W. (2010), Changes in the timing of snowmelt and streamflow in Colorado: A response to recent warming, *J. Clim.*, *23*, 2293–2306, doi:10.1175/2009JCLI2951.1.
Creed, I. F., and L. E. Band (1998a), Exploring functional similarity in the export of nitrate-N from forested catchments: A mechanistic modeling approach, *Water Resour. Res.*, *34*, 3079–3093, doi:10.1029/98WR02102.
Creed, I. F., and L. E. Band (1998b), Export of nitrogen from catchments within a temperate forest: Evidence for a unifying mechanism regulated by variable source area dynamics, *Water Resour. Res.*, *34*, 3105–3120, doi:10.1029/98WR01924.
Creed, I. F., L. E. Band, N. W. Foster, I. K. Morrison, J. A. Nicolson, R. S. Semkin, and D. S. Jeffries (1996), Regulation of nitrate-N release from temperate forests: A test of the N flushing hypothesis, *Water Resour. Res.*, *32*, 3337–3354, doi:10.1029/96WR02399.
Dunne, T., and L. B. Leopold (1978), *Water in Environmental Planning*, 818 pp., W. H. Freeman, San Francisco, Calif.
Elser, J. J., T. Andersen, J. S. Baron, A. Bergström, M. Jansson, M. Kyle, K. R. Nydick, L. Steger, and D. O. Hessen (2009), Shifts in lake N:P stoichiometry and nutrient limitation driven by atmospheric nitrogen deposition, *Science*, *326*, 835–837.
Erickson, T. A., M. W. Williams, and A. Winstral (2005), Persistence of topographic controls on the spatial distribution of snow in rugged mountain terrain, Colorado, United States, *Water Resour. Res.*, *41*, W04014, doi:10.1029/2003WR002973.
Flerchinger, G. N., W. Xaio, D. Marks, T. J. Sauer, and Q. Yu (2009), Comparison of algorithms for incoming atmospheric, long-wave radiation, *Water Resour. Res.*, *45*, W03423, doi:10.1029/2008WR007394.
Heuer, K., P. D. Brooks, and K. A. Tonnessen (1999), Nitrogen dynamics in two high elevation catchments during spring snowmelt 1996, Rocky Mountains, Colorado, *Hydrol. Processes*, *13*, 2203–2214.
Hewlett, J. D., and A. R. Hibbert (1967), Factors affecting the response of small watersheds to precipitation in humid areas, in *Forest Hydrology*, pp. 275–291, Pergamon, N. Y.
Idso, S. B. (1981), A set of equations for full spectrum and 8- to 14-micron and 10.5- to 12.5-micron thermal radiation from cloudless skies, *Water Resour. Res.*, *17*, 295–304.
Jepsen, S. M., N. P. Molotch, M. W. Williams, K. E. Rittger, and J. O. Sickman (2012), Interannual variability of snowmelt in the Sierra Nevada and Rocky Mountains, United States: Examples from two alpine watersheds, *Water Resour. Res.*, *48*, W02529, doi:10.1029/2011WR011006.
Johannessen, M., and A. Henriksen (1978), Chemistry of snow meltwater: Changes in concentration during melting, *Water Resour. Res.*, *14*, 615–619.
Kramer-Huth, A., A. Leydecker, J. O. Sickman, and R. C. Bales (2004), A two-component hydrograph separation for three high-elevation catchments in the Sierra Nevada, California, *Hydrol. Processes*, *18*(9), 1721–1733.
Liu, F., M. W. Williams, and N. Caine (2004), Source waters and flow paths in an alpine catchment, Colorado Front Range, United States, *Water Resour. Res.*, *40*, W09401, doi:10.1029/2004WR003076.
Magnusson, J., T. Jonas, I. Lopez-Moreno, and M. Lehning (2010), Snow cover response to climate change in a high alpine and half-glacierized basin in Switzerland, *Hydrol. Res.*, *41*, 230–240.
Marks, D., J. Domingo, D. Susong, T. Link, and D. Garen (1999), A spatially distributed energy balance snowmelt model for application in mountain basins, *Hydrol. Processes*, *13*, 1935–1959.
Martinec, J., and A. Rango (1981), Areal distribution of snow water equivalent evaluated by snow cover monitoring, *Water Resour. Res.*, *17*, 1480–1488.
McClain, M. E., et al. (2003), Biogeochemical hot spots and hot moments at the interface of terrestrial and aquatic ecosystems, *Ecosystems*, *6*, 301–312.
Meixner, T., and R. C. Bales (2003), Hydrochemical modeling of coupled C and N cycling in high-elevation catchments: Importance of snow cover, *Biogeochemistry*, *62*, 289–308.
Meixner, T., R. C. Bales, M. W. Williams, D. H. Campbell, and J. S. Baron (2000), Stream chemistry modeling of two watersheds in the Front Range, Colorado, *Water Resour. Res.*, *36*, 77–87.
Molotch, N. P. (2009), Reconstructing snow water equivalent in the Rio Grande headwaters using remotely sensed snow cover data and a spatially distributed snowmelt model, *Hydrol. Processes*, *23*, 1076–1089, doi:10.1002/hyp.7206.
Molotch, N. P., and R. C. Bales (2006), Comparison of ground-based and airborne snow surface albedo parameterizations in an alpine watershed: Impact on snowpack mass balance, *Water Resour. Res.*, *42*, 1–12.
Molotch, N. P., T. H. Painter, R. C. Bales, and J. Dozier (2004), Incorporating remotely-sensed snow albedo into a spatially-distributed snowmelt model, *Geophys. Res. Lett.*, *31*, L03501, doi:10.1029/2003GL019063.
Molotch, N. P., T. Meixner, and M. W. Williams (2008), Estimating stream chemistry during the snowmelt pulse using a spatially-distributed, coupled snowmelt and hydrochemical modeling approach, *Water Resour. Res.*, *44*, W11429, doi:10.1029/2007WR006587.
Mote, P. W. (2006), Climate-driven variability and trends in mountain snowpack in western North America, *J. Clim.*, *19*, 6209–6220.
Painter, T. H., J. Dozier, D. A. Roberts, R. E. Davis, and R. O. Green (2003), Retrieval of subpixel snow-covered area and grain size from imaging spectrometer data, *Remote Sens. Environ.*, *85*, 64–77.
Painter, T. H., K. Rittger, C. McKenzie, P. Slaughter, R. E. Davis, and J. Dozier (2009), Retrieval of subpixel snow covered area, grain size, and albedo from MODIS, *Remote Sens. Environ.*, *113*, 868–879.
Saros, J. E., K. C. Rose, D. W. Clow, V. C. Stephens, A. B. Nurse, H. A. Arnett, J. R. Stone, C. E. Williamson, and A. P. Wolfe (2010), Melting alpine glaciers enrich high-elevation lakes with reactive nitrogen, *Environ. Sci. Technol.*, *44*(13), 4891–4896.
Sickman, J. O., A. Leydecker, and J. M. Melack (2001), Nitrogen mass balances and abiotic controls on N retention and yield in high-elevation catchments of the Sierra Nevada, California, United States, *Water Resour. Res.*, *37*, 1445–1461.
Sickman, J. O., J. M. Melack, and J. L. Stoddard (2002), Regional analysis of inorganic nitrogen yield and retention in high-elevation ecosystems of the Sierra Nevada and Rocky Mountains, *Biogeochemistry*, *57*, 341–374.
Sickman, J. O., A. Leydecker, C. C. Y. Chang, C. Kendall, J. M. Melack, D. M. Lucero, and J. Schimel (2003a), Mechanisms underlying export of N from high-elevation catchments during seasonal transitions, *Biogeochemistry*, *64*, 1–24.
Sickman, J. O., D. Clow, and J. M. Melack (2003b), Evidence for nutrient enrichment of high-elevation lakes in the Sierra Nevada, California, *Limnol. Oceanogr. Methods*, *48*, 1885–1892.
Slater, A. G., M. P. Clark, and A. P. Barrett (2009), Comment on "Estimating the distribution of snow water equivalent using remotely sensed snow cover data and a spatially distributed snowmelt model: A multi-resolution, multi-sensor comparison" by N. P. Molotch and S. A. Margulis, *Adv. Water Resour.*, *32*, 1680–1684, doi:10.1016/j.advwatres.2009.09.001.

Slater, A. G., A. P. Barrett, M. P. Clark, J. D. Lundquist, and M. S. Raleigh (2013), Uncertainty in seasonal snow reconstruction: Relative impacts of forcing and image availability, *Adv. Water Resour.*, *55*, 165–177, doi:10.1016/j.advwatres.2012.07.006.

Tonnessen, K. A. (1991), The Emerald Lake watershed study: Introduction and site description, *Water Resour. Res.*, *27*, 1537–1539.

Williams, M. W., and J. M. Melack (1991a), Precipitation chemistry in and ionic loading to an alpine basin, Sierra Nevada, *Water Resour. Res.*, *27*, 1563–1574.

Williams, M. W., and J. M. Melack (1991b), Solute chemistry of snowmelt and runoff in an alpine basin, Sierra Nevada, *Water Resour. Res.*, *27*, 1575–1588.

Williams, M. W., J. S. Baron, N. Caine, R. Sommerfield, and R. Sanford (1996a), Nitrogen saturation in the Rocky Mountains, *Environ. Sci. Technol.*, *30*, 640–646.

Williams, M. W., P. D. Brooks, A. Mosier, and K. A. Tonnessen (1996b), Mineral nitrogen transformations in and under seasonal snow in a high-elevation catchment in the Rocky Mountains, United States, *Water Resour. Res.*, *32*, 3161–3171.

Williams, M. W., M. Losleben, N. Caine, and D. Greenland (1996c), Changes in climate and hydrochemical responses in a high-elevation catchment in the Rocky Mountains, USA, *Limnol. Oceanogr.*, *41*, 939–946.

Williams, M. W., T. Davinroy, and P. D. Brooks (1997), Organic and inorganic nitrogen pools in talus fields and subtalus water, Green Lakes Valley, Colorado Front Range, *Hydrol. Processes*, *11*, 1747–1760.

Williams, M. W., M. Knauf, N. Caine, F. Liu, and P. L. Verplanck (2006), Geochemistry and source waters of rock glacier outflow, Colorado Front Range, *Permafrost Periglacial Processes*, *17*, 13–33.

Williams, M. W., C. Seibold, and K. Chowanski (2009), Storage and release of solutes from a subalpine seasonal snowpack: Soil and stream water response, Niwot Ridge, Colorado, *Biogeochemistry*, *95*(1), 77–94, doi:10.1007/s10533-009-9288-x.